Advancements of Intense Terahertz Field Focusing on Metallic Nanoarchitectures for Monitoring Hidden Interatomic Gas-Matter Interactions

Jinwoo Lee, Jongsu Lee, Geon Lee, Dai-Sik Kim, Yong-Sang Ryu,* and Minah Seo*

With the advancements of nanotechnology, innovative photonic designs coupled with functional materials provide a unique way to acquire, share, and respond effectively to information. It is found that the simple deposition of a 30 nm-thick palladium nanofilm on a terahertz (THz) metasurface chip with a 14 nm-wide effective nanogap of asymmetric materials and geometries allows the tracking of both interatomic and interfacial gas–matter interactions, including gas adsorption, hydrogenation (or dehydrogenation), metal phase changes, and unique water-forming reactions. Combinatorial analyses by simulation and experimental measurements demonstrate the distinct nanostructures, which leads to significant light-matter interactions and corresponding THz absorption in a real-time, highly repeatable, and reliable manner. The complex lattice dynamics and intrinsic properties of metals influenced by hydrogen gas exposure are also thoroughly examined using systematically controlled ternary gas mixture devices that mimic normal temperature and pressure. Furthermore, the novel degrees of freedom are utilized to analyze various physical phenomena, and thus, analytical methods that enable the tracking of unknown hidden stages of water-forming reactions resulting in water growth are introduced. A single exposure of the wave spectrum emphasizes the robustness of the proposed THz nanoscopic probe, bridging the gap between fundamental laboratory research and industry.

1. Introduction

Terahertz (THz) technology is a powerful optical sensing platform that provides highly precise methodologies for the real-time navigation of intrinsic materials in a noncontact manner. It offers considerable information, including the full vectorial components of field magnitudes and phases. Thus, it provides a direct evaluation of the permittivity,[1] permeability,[2] and conductivity[3] of materials with various molecular fingerprint properties for spectroscopic purposes.[4–6] In recent years, remarkable advances in nanotechnology have led to significant increases in sensitivity and selectivity, which are key factors in sensing research.[7] These advances have helped overcome the severe diffraction and absorption cross-section limitations of long-wavelength light.[8] The emergence of metasurfaces realized with geometrically defined subwavelength resonances combined with a biochemical material coating over the functional surface has enhanced the molecular sensitivity of THz

J. Lee, J. Lee, G. Lee, M. Seo
Sensor System Research Center
Korea Institute of Science and Technology
Seoul 02792, Republic of Korea
E-mail: mseo@kist.re.kr
J. Lee, M. Seo
KU-KIST Graduate School of Converging Science and Technology
Korea University
Seoul 02841, Republic of Korea
J. Lee
Department of Electrical Engineering and Computer Science
Northwestern University
Evanston, IL 60208, USA

G. Lee, D.-S. Kim
Department of Physics and Astronomy
Seoul National University
Seoul 08826, Republic of Korea
G. Lee, D.-S. Kim
Department of Physics
Long-wavelength Nanotechnology Laboratory
and Quantum Photonics Institute
Ulsan National Institute of Science and Technology (UNIST)
Ulsan 44919, Republic of Korea
Y.-S. Ryu
School of Biomedical Engineering
Korea University
Seoul 02841, Republic of Korea
E-mail: rongxiang82@korea.ac.kr
Y.-S. Ryu
Interdisciplinary Program in Precision Public Health
Korea University
Seoul 02841, Republic of Korea

**ADVANCED
SCIENCE NEWS**

www.advancedsciencenews.com

**ADVANCED
MATERIALS**

www.advmat.de

waves. This bypasses the length mismatch between the scales of molecules and THz wavelengths. Metasurfaces include split-ring resonators, Fano-resonance structures, and dipole antennas.[9] Furthermore, the complementary structural options of positive and negative patterns,[10] material hybridization, and surface treatment[11] have extended their applications to a broader range. Other optical sensing methodologies analyze the resonance shift behaviors affected by the surrounding medium; however, THz waves employ complex refractive indices and geometrical changes as critical parameters for tracking complicated multistage transitions.[12–14] For this, nano-structured metasurfaces can be used for unveiling the underlying dynamics. This can be achieved with high-precision monitoring of target objects and materials via complementary information of resonance shifts and transmittance modulations by converting free-propagating radiation into strongly squeezed fields inside the nano-volume.

For instance, f or monitoring gas–matter interactions and generating atomically small substances via a catalytic reaction, a gas-responsive metal as a sensing pad is a suitable candidate using THz technology. Palladium (Pd) is a perfect example owing to its high reactivity with hydrogen gas, inducing palladium hydride (PdH), and low activation energy for investigating gas adsorption, atomic dissociation, and diffusion at room temperature.[15,16] Spontaneous phase transition to PdH occurs under specific hydrogen concentrations. This phase transition is accompanied by significant Pd volume expansion and Fermi-level shifts of conduction electrons, which modify the metal permittivity, permeability, and conductivity.[17,18] Various high-tech equipment, such as scanning photoemission microscopy (SPM)[19] and transmission electron microscopy (TEM),[20,21] are used to study atomic-scale catalytic interfacial molecular reactions; however, their restricted operating vacuum modes or template loading conditions limit the in situ probing of gas–matter interactions occurring in atmospheric environments. Real-time X-ray Diffraction (XRD) enables the tracking of interatomic fusionic gas interactions in crystalline metal lattices[22,23]; however, studying interfacial kinetic reactions (such as catalytic reactions) still requires SPM or TEM measurements.[24] To compensate for these issues, only simulation calculations, such as density functional theory (DFT), have been performed, which are yet to be experimentally confirmed by considering both interatomic and interfacial modulations under gas–matter interactions. However, such a direct approach of using metals for THz nanotechnology is difficult owing to the absence of spectral characteristics in the THz band and its shallow penetration depth. Most metals have drude-like properties, which prevent electromagnetic waves from penetrating deeper than the skin depth ($\delta \sim 100$ nm). Only a small portion of such metals can interact with THz waves; therefore, specialized structures are required to achieve high sensing efficiency for metal detection.

In this study, we demonstrated an asymmetrically positioned heteronanogap structure that achieved extremely high sensitivity for THz optical detection, even for metals. Among the diverse metasurface structures, slot antennas with a high aspect ratio (length-to-width) have significant advantages in terms of large-field amplification and squeezed mode volume.[25] When the gap width is lesser than the skin depth, the correlated evanescent mode on both sides of the metal wall, known as the gap plasmon

mode, generates an enormous inductive current. This feature enhances the light-metal interaction through ohmic absorption; consequently, observing the states of metals in the THz spectrum became possible. With a relatively large difference in optical properties during metal transitions in the THz range and enhanced light-metal interactions (such as metal absorption), THz technology with a specific metamaterial structure is substantially effective for investigating the dynamics of metal transitions. Thus, we showed the in situ probing of the hydrogen interfacial and intra-atomic dynamics of transition metals under controlled gas environments and unique water-forming reactions in an atmospheric environment. These dynamics were experimentally examined using metasurface-assisted nanoscopic THz measurements. Considering that THz waves are significantly absorbed by water molecules, real-time THz measurements are exceptionally suitable for studying the distinctive water-forming reactions facilitated by Pd catalysts. Based on quantitative analysis using the effective gap approximation for simulations, we propose methodological approaches for the real-time analysis of gas-matter interactions, such as physical adsorption, phase transition, and sequential volumetric interatomic expansion, in a repeatable and reliable manner. Furthermore, we investigated the unknown hidden stage of water-forming reactions, followed by water growth, with a single exposure to the THz wave spectrum.

2. Results and Discussion

2.1. Nanogap-Induced THz-Field Amplification for Monitoring Gas-Assisted Interatomic Dynamics

The experimental scheme describes the basic concept of broadband THz spectroscopy combined with nanoscale metasurface sensing chips for significantly enhancing atomic sensitivity (**Figure 1**a). For real-time tracking of geometric and material property changes in a lattice with atomic-scale sensitivity, we used THz spectroscopy combined with functional metasurfaces with Pd nanofilm deposited nanoslots. The 10 nm-thick titanium (Ti) layer was placed underneath the 20 nm-thick Pd to supplement the system reproducibility (Figure S1, Supporting Information).[26] A THz metasurface chip with nanoslot arrays was fabricated uniformly and reliably, as confirmed by a top-view of an optical micrograph (Figure 1b), and a pseudo-color cross-sectional scanning electron microscopy (SEM) image that demonstrated the well-designed nanogaps (Figure 1c). Infinitesimal gap volumes between the asymmetric gold (Au) wall and metallic Pd edges of each nanoslot effectively created ≈14 nm-wide gaps. This structure substantially increased THz field at such a nanoscale mode volume. This enabled the detection of signals as small as ≈10 nm in the millimeter-scale probing area. To induce better detectability, the nanogap distance, which is directly related to the capacitive effect, and Pd film thickness, and the nanoscale mode volume described as Purcell factor ($F_p \approx 8.97 \times 10^8 \, (n/\lambda)^3$), were considered for designing the metasurface (Figure S2, Supporting Information). Moreover, the high-energy absorption of the Pd pad induced by the asymmetric structure between 150 nm-thick Au and 30 nm-thick Pd/Ti nanofilm enabled sensitive measurement of the optical property changes of Pd. Consequently, microscopic monitoring and tracking of gas–matter interactions and dynamics in the macroscopic area
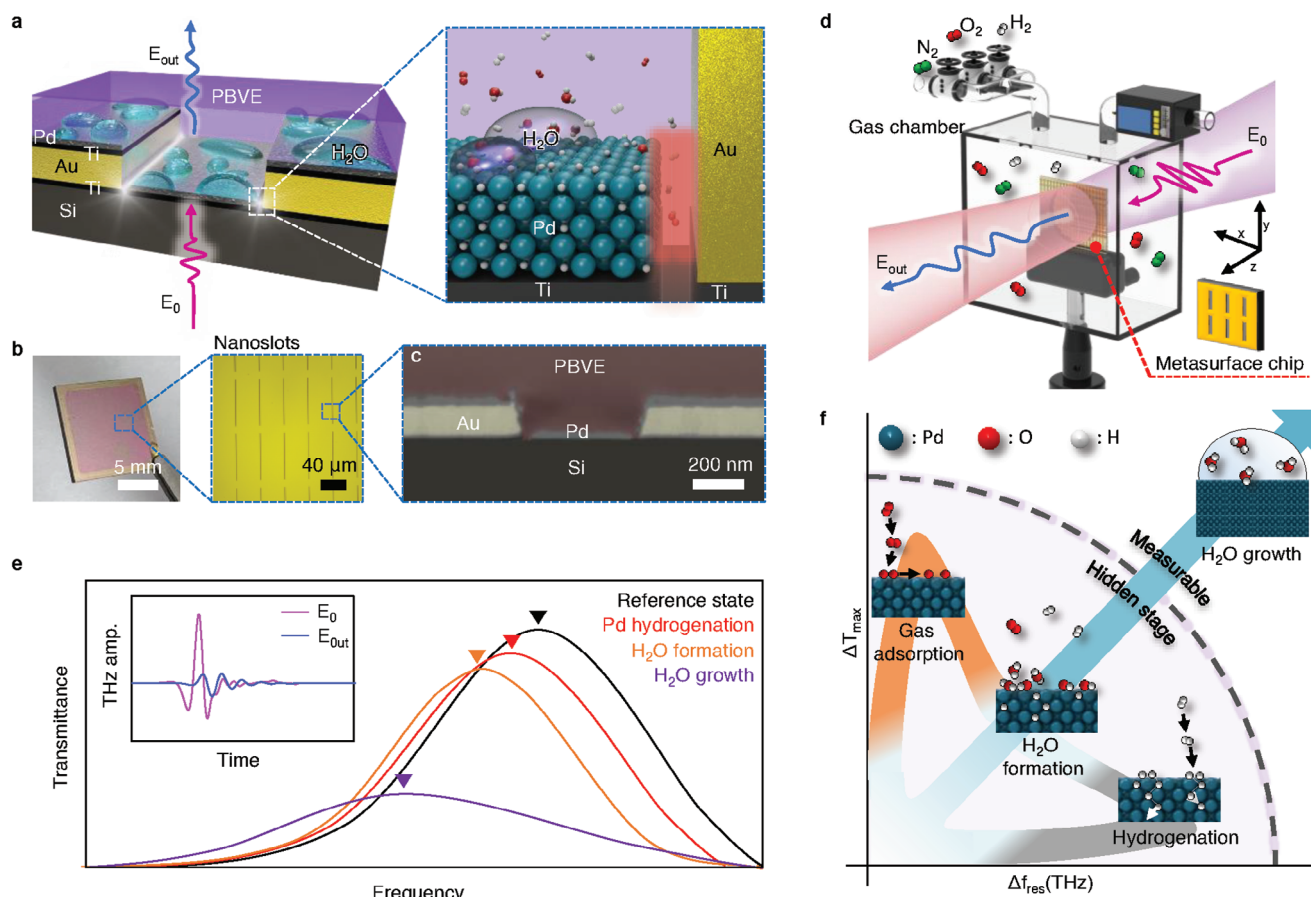
2308975 (2 of 11)

Figure 1. THz metasurface chip for monitoring atomic transition under gas exposure. a) THz metasurface chip enabling the squeezing of incident THz fields at the confined THz optical hot-spot: nanogap. Coating of perfluoro(butenyl vinyl ether) (PBVE) polymer membrane over the metasurface chip enables water accumulation at the PBVE/Pd interface owing to suppressed interfacial water evaporation. b) Top view of an optical image of THz metasurface chip (left) and an enlarged area with nanoslot arrays captured in a microscopic bright-field image (right). c) Cross-sectional SEM image of a single unit of nanoslot, revealing the nanogap between the Au wall and Pd pad. d) Measurement setup for in situ THz monitoring under various ambient conditions. e) Conceptual of THz spectra for metasurface chips during four different states via Fourier transform. The inset figure shows expected of THz field amplitude in the time-domain for incident (E_0) and transmitted signals (E_{out}) through metasurface chips. f) Conceptual illustration of the THz monitoring of early hidden states including gas adsorption, interatomic hydrogen reaction, and interfacial water forming process.

beyond the diffraction limit and absorption cross-sectional limit was realized.

As shown in the THz measurement setup (Figure 1d), the transmitted THz field (E_{out}) in the time domain was measured in various ambient gases, including H_2, O_2, and N_2 (Experimental Section). The incident THz wave (E_0) was polarized along the x-axis when the longer axis of the nanoslot was along the y-axis. To monitor the lattice dynamics during Pd hydrogenation, the THz metasurface chip was housed in a chamber to mimic the atmospheric environment via an N_2, O_2, and H_2 gas-controlled system (Experimental Section). The transmittances in the frequency domain were continuously obtained every 3 s for a real-time step resolution. The measured E_{out} of the metasurface chip (under specific gas conditions) was then divided by that of the bare silicon substrate without the metasurface and converted to frequency-domain data using a fast Fourier transform (FFT) for extracting the transmittance value (Figure S3, Supporting Information). To investigate the dynamic responses, we tracked the change of resonance frequency (f_{res}) and maximum transmit-

tance (T_{max}) located at the resonance frequency. The significant advantages of our methodology for achieving effective THz signal extraction, with a measurable minimal signal of the transmittance of 0.001 and resonance frequency of 0.5 GHz, from noise signals are discussed in Figure S4, Supporting Information. Various Pd-gas interactions under different gas conditions are conceptually expressed as FFT-treated spectral forms (Figure 1e). The THz spectrum can be interpreted in terms of two important parameters, resonance shift ($\Delta f_{res} = (f_{res}\ (t) - f_{res}(t=0))$) and transmittance change ($\Delta T_{max} = -\ (T_{max}\ (t) - T_{max}(t=0))$) at a given time, t. The relative changes in the latter further explain various physical/chemical reactions including Pd hydrogenations, H_2O formation, and H_2O growth as denoted by different colored-curves.

A negative control experiment using a Pd-free THz nanoslot chip under identical hydrogen modes was conducted. The experiment confirmed that the THz signals arose solely from the phase transition of Pd and not directly from the environmental gas molecules (Figure S5, Supporting Information). Overall, to obtain the maximum signal-to-noise ratio (SNR) during THz

**ADVANCED
SCIENCE NEWS**

www.advancedsciencenews.com

**ADVANCED
MATERIALS**

www.advmat.de

measurements for different purposes, two types of resonance chips with distinct nanoslot structures were designed: 0.83 and 1.17 THz chips for investigating the in situ Pd phase transition (hydrogenation) and effectively monitoring interfacial nano-volumetric H_2O films, respectively. This is because the metal-transition induced lattice dynamics of the Pd were expected to be measurable in the range of 0.82–0.83 THz with maximum systemic SNR, whereas H_2O molecules had a broad absorption with a coefficient of 230 cm^{-1} at 1.17 THz. Both THz nanoslots were coated with perfluoro(butenyl vinyl ether) (PBVE) polymer mixtures (PBVE polymer in a fluorosolvent), which completely filled the entire space within the nanoslots without any volumetric vacancies (Experimental Section).

From a single H_2O molecule to a crowded population and the subsequent bulky H_2O formation, water consisting of atoms (i.e., H and O) experiences multiple potential paths that are obscured and inscrutable (Figure 1f). To reveal the underlying pathway and lattice dynamics inside this hidden stage, we proposed a THz methodology via scattering resonance features in the Δf_{res} and ΔT_{max} domains. This should help uncover the initial hidden state, leading to further investigations of various gas–metal interactions and their behavioral dynamics. In particular, Pd–gas interactions, such as oxygen adsorption, interatomic hydrogen reactions, and interfacial water-forming processes, occur at an early stage.

2.2. Structural Design of an Effective Nanogap for Optimal Performance

To enhance the detectability of Pd-gas interactions, it is crucial to understand the gap plasmon mode at the Au/Pd interface, and their optimized physical properties such as metal thickness (h) and width (w). The field enhancement near the gap is a key factor in the gap plasmon effect, which affects the resonance frequency and transmittance change; thus, we optimized the metasurface structure to yield the highest field enhancement. As mentioned previously, a narrower gap is more efficient in significantly improving the field according to the capacitive nature (Figure 1; Figure S6, Supporting Information). However, the influence of the nanofilm thickness may add to the complexity. While a thinner structure aids in spatially confining the field, a counterintuitive trend exists in which the field enhancement decreases with decreasing metal thickness. Consequently, the design of metasurface sensors requires a comprehensive understanding of correlation between the field enhancement and the shape and size of the structure.

Recently, the gap plasmon was demonstrated in extremely narrow gaps below the skin depth ($w < \delta$); its behavior is influenced by the substrate permittivity.[27] To assess the effect of metal thickness on the electric field, finite element method (FEM) simulations were conducted by considering Au and Pd/Ti thickness variations (h_{Au} and h_{Pd}, respectively). The thickness of each metal was varied from 30 to 150 nm near the gap plasmon regime ($w < h$). The calculated field distributions are shown for symmetric configurations for h_{Au} and h_{Pd} = 150 and 30 nm (**Figure 2**a,b, respectively) and asymmetric configurations for h_{Au} = 150 nm and h_{Pd} = 30 nm (Figure 2c). As observed, the field enhancement maximized when the thickness was significantly greater

($h \gg w$) than the gap width in the symmetric structure (black line in Figure 2d), and field enhancement diminished when both h_{Au} and h_{Pd} were 30 nm (red line in Figure 2d). Conversely, the asymmetric structure achieved both substantial field augmentation (enhanced by > 1000) and compression of the spatial mode volume (sub-microvolume). Moreover, the asymmetric design proved to be particularly advantageous for enhancing Pd absorption. As shown in Figure 2e, the THz absorption per unit volume ($P_{abs,Pd}/V$) of the middle Pd pad was calculated. The absorption changed barely for the metal thickness of greater than skin depth ($h > \delta$) since only surface charge contributes to the energy extinction. However, when the metal thickness was less than skin depth ($h < \delta$), the absorption increased exponentially since the overall internal charge contributed to increased absorption.[28] Although the absorption perpetually increased as h_{Pd} decreased (along the black line in Figure 2e), having a specific thickness was necessary to ensure film quality. According to previous research, Pd achieves bulk-level conductivity above a thickness of at least 30 nm.[29] Given the film quality and conductivity reduction through the nanoscale effect, the absorption of the Pd film would be diminished in the 30 nm region (dashed lines in Figure 2e). Hence, the 30 nm Pd with the 150 nm Au slot represents the most favorable design for our purpose. In particular, as shown in Figure 2e, the absorption of the Pd film was greater in the asymmetric structure than in the symmetric structure as h_{Pd} decreased. These results indicate the ultimate advantages of the asymmetric structure being a metal sensor, owing to its high absorptivity. The asymmetric case (orange line in Figure 2e) showed higher metal absorption than the symmetric case (black line in Figure 2e), along with a small mode volume. Moreover, despite the asymmetrical decrease in h_{Pd}, it still demonstrated a high field enhancement. Further information on the field enhancement and absorption of the aforementioned structures is presented in Figure S7, Supporting Information

To examine the actual performance of the proposed sensing chip, we simulated absorption changes during the catalytic reaction. The intrinsic bare Pd film undergoes a phase transition (α-phase to β-phase) under H_2 exposure.[30–32] In particular, the intrinsic properties of the Pd change as a result of phase transition. First, the H_2 gas induced phase of the Pd film (Figure S8, Supporting Information). The THz absorption was then calculated for each Pd status. The absorption difference was apparently significant despite the small THz property difference between Pd and PdH. This was more obvious compared with the symmetric case (Figure 2e). Surprisingly, the estimated difference (ΔP_{abs}) was comparable to the transmittance change (ΔT_{max}). This indicates that the THz transmission is originated from the phase change of Pd. Notably, the optimized asymmetric structure resulted in a greater reduction in transmittance than the symmetric structure (Figure 2f). In summary, the asymmetric structure with h_{Au} = 150 nm and h_{Pd} = 30 nm emerges as the optimal candidate for investigating light-matter interactions, attributed to its notable field enhancement, compressed mode volume, and high ohmic absorptivity when compared to symmetric structures. Consequently, the phase transformation of the material was discernible by tracking the transmittance of the structure. In addition to the aforementioned advantages, the strong field enhancement and substantially small mode volume enabled the detection of catalytic reaction products.
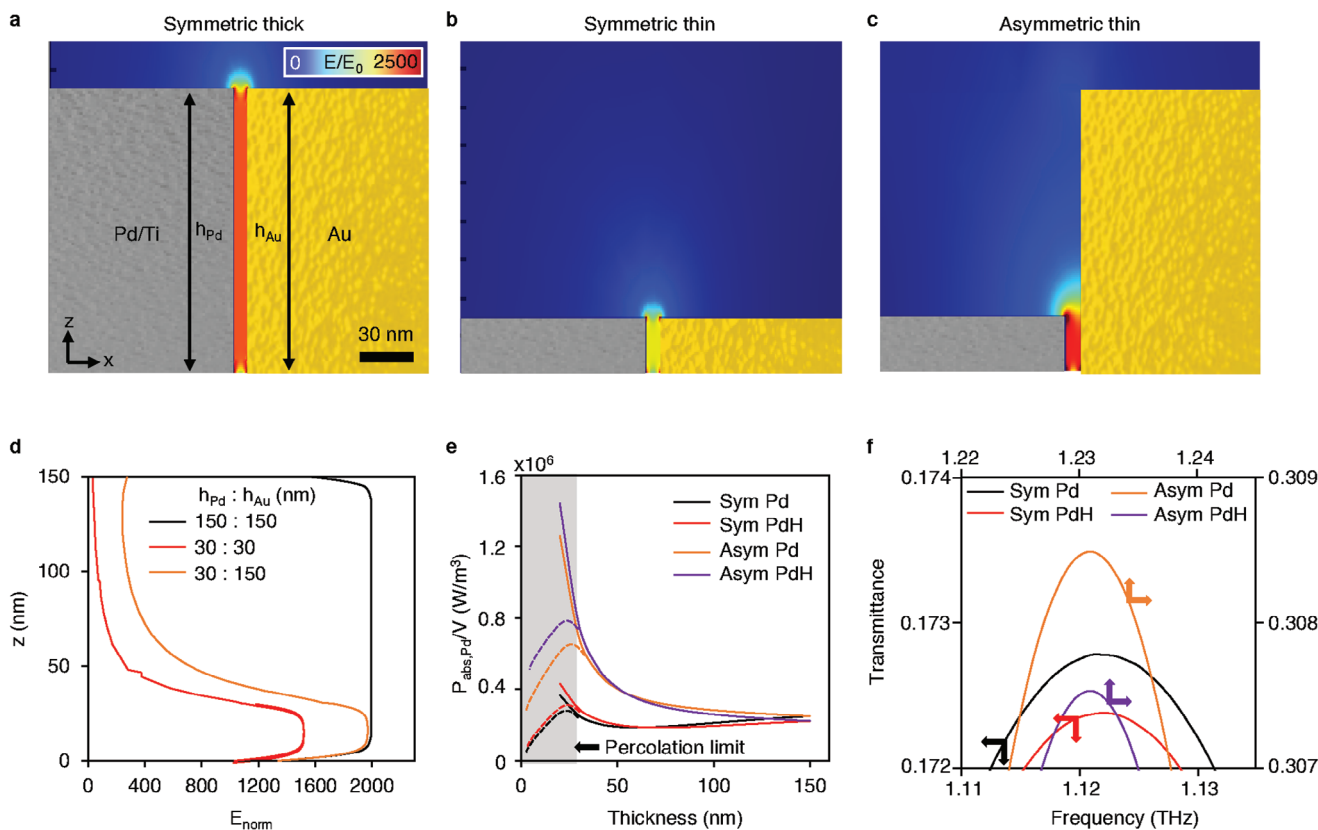
Figure 2. Computational optimization of the structural configuration. a–c) Calculated THz field distribution at the nanogap exhibiting symmetric structure of both 150 nm-thick Pd and Au (a), 30 nm-thick Pd and Au (b), and asymmetric structure of 30 nm-thick Pd and 150 nm-thick Au, respectively (c). d) Evaluated normalized THz field at the nanogap along the z-axis. e) Determined absorption per volume values of Pd pad ($P_{abs,Pd}/V$) according to the thickness of the Pd film. f) Transmittance change for symmetric and asymmetric structure when the Pd pad is at Pd and PdH states. The colored arrow depicts the axes of each structure. The scale bar in (a) also applies to (b) and (c).

2.3. In Situ THz Responses to Pd Phase-Transition

Next, we applied the proposed metal structure to a real case. THz transmission was measured for a period of time during H_2 gas exposure. As expected, the resultant transmission varied with the H_2 concentration (**Figure 3**a). Another aspect to consider is the resonance frequency, which provides additional information. As the Pd film transitions to PdH, the volume expansion by Pd hydrogenation narrows the nanogap (w_g to w_g' in Figure 3b).[33–35] This nanogap narrowing effect induces more charges at the metal surface like a capacitor; thus, a stronger E-field across the metal plates causes the THz wave to concentrate at the optical hotspot.[25] For cross-validation, we defined an effective gap model to simulate the structural base of the Pd configuration within the nanoslots (Figure S9, Supporting Information) and investigated the impact of the nanogap width w_g on the THz field distribution and f_{res} response. The resonance frequency changes, strongly associated with the gap capacitance (C) and inductance (L) ($f_{res} \sim 1/2\pi\sqrt{LC}$), were highly affected by w_g reductions. The calculated THz field distribution represented its enhancement to an incidence of average 1 850 in amplitude (3.42×10^6 in intensity), inducing a further enhancement of ≈ 80 in the absorption cross-section. Consequently, the extremely en-

hanced sensitivity of such a well-controlled geometry enabled the detection of lattice dynamics, such as Pd hydrogenation. These simulations were crucial for interpreting further experimental observations in terms of the gap width.

Given that our measurements were conducted under isothermal conditions, the data measured during hydrogenation can be compared with extensively studied XRD results.[36] The Pd/PdH transition with respect to H_2 pressure during gas absorption/desorption can be explained in terms of Δf_{res}, with the fact that the lattice status is critically responsible for the resonance behavior. We investigated the Pd transition by controlling the inlet gas composition (especially the H_2 concentration) for in situ monitoring of Pd hydrogenation (Figure S10, Supporting Information). With increasing H_2, a slight redshift of Δf_{res} from 0.827 to 0.823 THz was observed in the THz frequency domain data; the shifted signal was completely recovered after H_2 dilution. This demonstrated the reproducibility of our metasurface chip. As expected, two dramatic slope changes were measured, confirming the metal transition from a metallic film (α-phase) to a dielectric-like film (β-phase) under increasing H_2 gas pressure and vice versa (Figure 3c). This isotherm plot with a hysteresis and plateau ($\alpha+\beta$ phase) showed excellent correspondence with earlier studies.[37] In contrast to the miscibility gap upon H_2
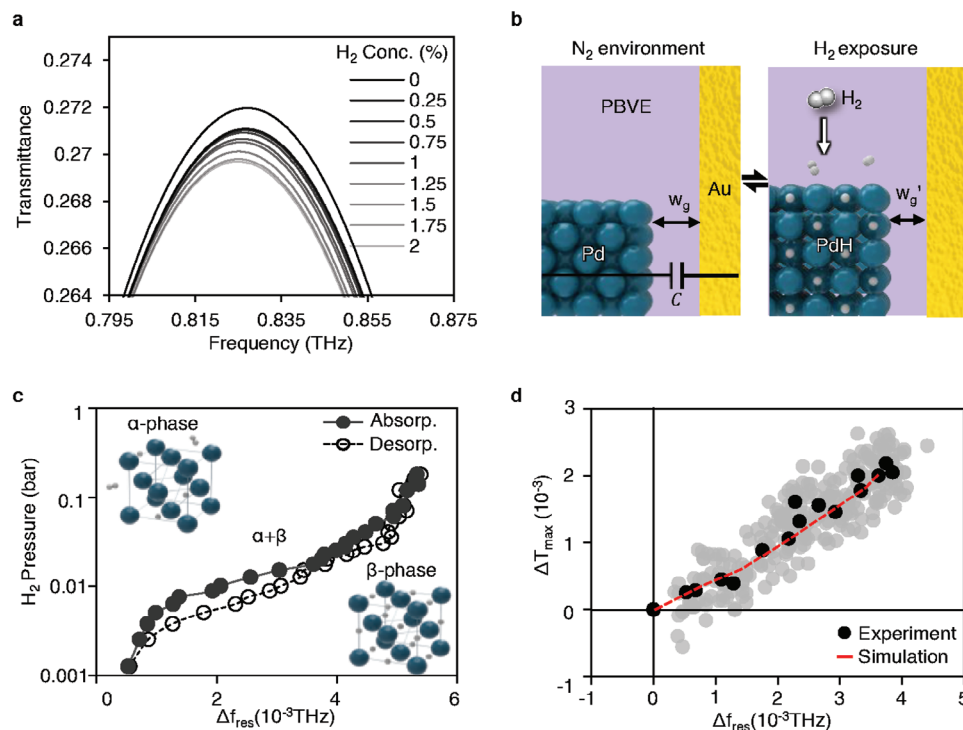
Figure 3. Real-time monitoring of Pd phase-transition under H_2 exposure. a) Measured spectral data sets under various hydrogen concentrations (ranging from 0.0 to 2.0% with a step of 0.25%) after FFT treatment. b) Schematic illustration of resultant lattice expansion by Pd hydrogenation. A high capacitive field was caused by the induced current near the effective gap. The lattice expansion during hydrogenation perturbs the gap capacitance and the resonance frequency of the system. c) Δf_{res} response according to H_2 pressures, showing the hysteresis curve of the Pd-PdH system. d) Changes in f_{res} and T_{max} mapped during hydrogenation. The black spots represent the mean values of the measured Δf_{res} and ΔT_{max} (gray spots), while the red dashed line indicates the simulated Δf_{res} and ΔT_{max}.

absorption/desorption observed in bulky Pd metals,[22] the absence of such a hysteresis gap under identical H_2 conditions indicated that tens of nanometer-thin Pd film and the Ti adhesion layer hindered the $\alpha+\beta$ intermediate state.[38] On applying this Pd/Ti metal slab to the effective gap model, measured Δf_{res} values of 4–5 GHz were obtained from a 0.2 nm reduction in the gap width (w_g'). This verified the atomic-scale detectability of our system.

The detection reproducibility was tested by monitoring the time lapse of f_{res} responses under a gradual increase in H_2 concentration (Figure S11, Supporting Information). THz signals of different magnitudes measured during repeated injection/ventilation procedures demonstrated that the Pd/PdH transition processes were completely reversible, owing to the strong adhesive support of the Ti film (Figure S1, Supporting Information). Such an investigation using f_{res} response was useful for treating atomic-scale deviations, as f_{res} was relatively free from long-term system fluctuations (system noise) (Figure S11, Supporting Information). However, to expand our scope to various dynamic phenomena, including optical property changes, T_{max} values were considered. As mentioned earlier, although the obtained redshift of Δf_{res} was considered with lattice expansion only, optical properties of the Pd during the hydrogenation can be visualized with ΔT_{max} values. From the simulation with the extracted refractive index, both geometry and optical property changes were confirmed to produce a certain slope in the Δf_{res} versus ΔT_{max} map (Figure S12, Supporting Information). Excel-

lent agreement was observed between the measured THz signals (black circles) during Pd hydrogenation and corresponding simulation results (red dashed line) (Figure 3d). Further studies using the Δf_{res}-ΔT_{max} mapping will present a variety of transition dynamics, e.g., oxygen adsorption and nano-volume water formation.

2.4. In Situ THz Responses for Unveiling Hidden Gas–Metal Interactions: O_2 Adsorption, Pd Hydrogenation, and Water-Forming Reaction

After confirming the detection performance in tracking the interatomic metal transition during hydrogenation, we further monitored the interfacial gas–metal behavior using the proposed THz metasurface. Pd is a well-known catalyst that dissociates O_2/H_2 molecules into O/H atoms, forming H_2O films of nano-volume under specific gas combinations (**Figure 4**a). Combinatorial gas exposure on a THz metasurface enables the investigation of catalytic gas adsorption/absorption accompanied by H_2O formation and growth, which has not been experimentally demonstrated via optical approaches.[39] To this end, we set the mass flow controller system (Experimental Section) to supply 20% of O_2 (Figure 4b, red line) with varying H_2 (Figure 4b, green line, 0–9%) and N_2 for purging (not displayed), and measured THz signals every 3 s, and varied H_2 concentrations with 1% interval every 20 min for 205 min. The 1.17 THz chip was used to effectively
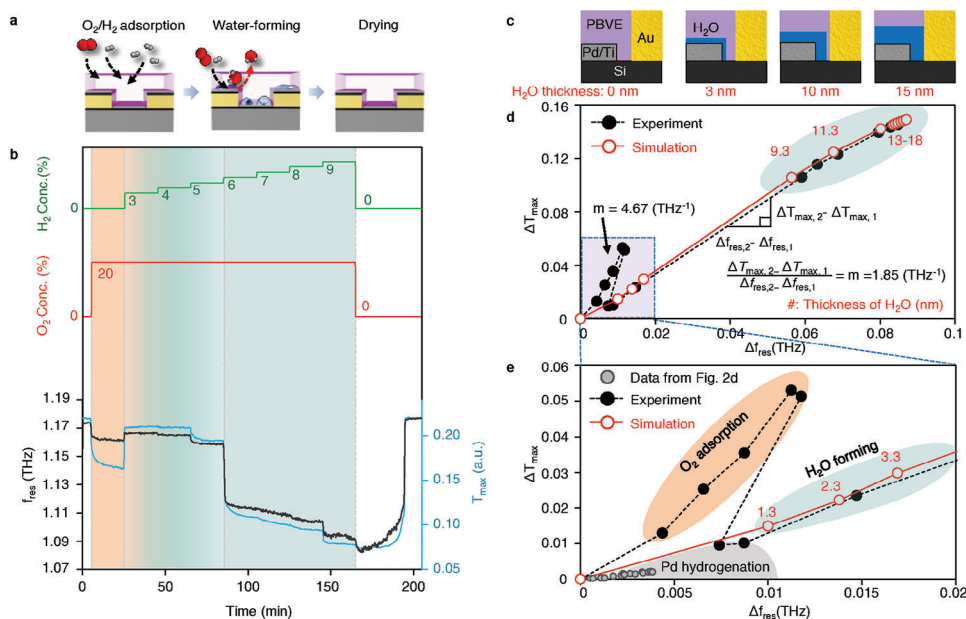
**ADVANCED
SCIENCE NEWS**

www.advancedsciencenews.com

**ADVANCED
MATERIALS**

www.advmat.de

Figure 4. Water-forming reactions at PBVE/Pd interface under additional O_2 exposure. a) Scheme showing the water-forming reaction at the PBVE/Pd interface. b) Time-lapse monitoring of f_{res} and T_{max} while varying exposing gas species and concentrations during water formation and growth. c) Scheme illustrating the water evolution at the PBVE/Pd interface. Note that red numbers denote simulated water film thickness contouring the Pd pad. d) Corresponding ΔT_{max} as a function of Δf_{res} from (b). Black and red dots represent experimental measurements and simulation values, respectively. e) Enlarged graph of (d) depicting the hidden stage of gas–metal interactions including oxygen adsorption, Pd hydrogenation and interfacial water formation.

monitor the volumetric H_2O film at the PBVE/Pd interfaces, based on our previous study.[40] The PBVE polymer coated onto Pd allowed gas-type molecules with different permeabilities for O_2, H_2, N_2, and H_2O, but strongly suppressed water evaporation (Figure S13, Supporting Information).[41] Notably, as depicted in Figure 4b, the T_{max} reduction (blue line, $5 < t < 25$ min) under a 20% O_2 supply was more significant than the f_{res} reduction (black line), showing a more drastic response compared to those measured under H_2 exposure. Regarding redshifts, Δf_{res} was more dominant than ΔT_{max} during Pd hydrogenation, and an inverse trend (sharper ΔT_{max} reduction than Δf_{res}) can be interpreted as the conductivity change of Pd surface by adsorption of O adhesives owing to the catalytic reaction of O_2.[42] This demonstrates the detectability of our THz metasurface for monitoring the interfacial chemistry of Pd pads.

Abrupt THz signal increases in both T_{max} and f_{res} were measured after H_2 injections ($t = 25$ min), showing an excellent correspondence to the fact that the stronger chemisorption of H than O results in the replacement of O adhesives with H adhesives.[43,44] The change in the THz signal at $t > 25$ min ($H_2:O_2 = 3:20$) was measured stepwise as the amount of H_2 increased. When the H_2 concentration exceeded 6% ($t > 85$ min), a significant signal reduction was observed. In our previous study, under the same conditions, fluorescence interference contrast (FLIC) revealed an abrupt microscopic outbreak of water droplets and their growth owing to the merging with the neighboring droplets ($t > 85$ min, $H_2:O_2 = 6:20$).[45] This evolutionary shape change confirmed that the water growth reaction was the origin of the large THz signal reduction (Figure S14, Supporting Information).[40] However, the origin of the slight THz signal change at $25 < t < 85$ min ($H_2:O_2 = 3-6:20$) remained unclear.

For this, we conducted numerical simulations using the effective gap model and compared the results with the measured data at $25 < t < 160$ min. We assumed that a uniform H_2O film contoured the Pd surface for the effective volume of randomly dispersed water bubbles at the PBVE/Pd interface and that its growth modulated the H_2O film thickness (Figure 4c). Simulation results (red circles) were plotted together with the measured experimental data (black dots) as a function of Δf_{res} versus ΔT_{max} (Figure 4d). In the simulation, the newly formed H_2O nanofilm and its increased thickness produced a middle slope (red line), which matched the second scheme shown in Figure 4c, where the evaporation rate was still higher than or equal to the generation rate (Figure S15, Supporting Information). Paradoxically, this emphasizes the advantages of THz metasurface chips., i.e., monitoring trace amounts of H_2O nanofilms, even for extremely small amounts of H_2O (1–2 nm-thick-H_2O film), which are products of equal (or smaller) values of the H_2O generation ratio with respect to the H_2O evaporation ratio. Conversely, as the H_2 concentration increased to >6%, the water generation rate exceeded the evaporation rate (blue zone in Figure 4d), representing large values on the map, as described in the third scheme in Figure 4c. When the generated water occupied the entire nanogap space, it existed outside the most sensitive mode volume region, and the water-related signal was saturated (the fourth one in Figure 4c).

We focused on the reaction occurring at an extremely small-scale region at an early time and defined it as the "hidden stage." In this stage, the oxygen adsorption, nanoscale H_2O film formation, and interatomic hydrogen reaction of Pd were measured (Figure 4e). From the water line in the middle, the initially obtained experimental data under oxygen-only conditions are

**ADVANCED
SCIENCE NEWS**

www.advancedsciencenews.com

**ADVANCED
MATERIALS**

www.advmat.de

plotted on the upper side as O_2 adsorption (orange zone). As the amount of H_2 gas increased, the O atoms attached to the Pd surface fell out, and both the signals in f_{res} and T_{max} changed abruptly. As explained above, water nanofilms were formed below 6% H_2 concentration, and these data are plotted on the middle side (blue zone in Figure 4e). The "orange" and "blue" regions represent oxygen adsorption and nanoscale H_2O formation, respectively. The dark grey region, which is dominated by the resonance frequency shift, represents the interatomic hydrogen reaction (Figure 3d). Further studies of various reactions mapped in terms of scattered regions will help classify different transition dynamics and understand various behaviors under different gas atmosphere conditions.

2.5. Dehydrogenation and Water-Forming Dynamics at the PBVE/Pd Interface

As discussed previously (Figures 3 and 4; Figure S12, Supporting Information), a Δf_{res}-ΔT_{max} map provides detailed information for analyzing complex lattice or interfacial dynamics of the Pd metal influenced by exposed gas. A new experimental setup was used to examine the gas-induced complex dynamics of water-forming reactions. For this purpose, an increasing O_2 influx under 5% H_2 supply was exposed to the metasurface (**Figure 5**a; Figure S16, Supporting Information). Each step included Pd catalytic reaction followed by H_2O forming reaction, numbered in ① to ⑤. H_2O forming reactions-related processes were plotted along the middle line of the Δf_{res}-ΔT_{max} map (blue region, Figure 5b). The initial data jump from ① to ② in the Δf_{res}-ΔT_{max} map was attributed to the hydrogenation process ($m = (\Delta T_{max,2}-\Delta T_{max,1})/(\Delta f_{res,2} - \Delta f_{res,1}) = 0.5$ in Figure 5b). Under gradual increment of O_2 influx from 2% to 6%, the plotted data in Figure 5b increased with its mean slope ($m = 1.1$, ② to ③), showing a similar slope value in Figure 4e (water forming reaction). This implied that an ongoing H_2O formation reaction occurred under these gas conditions, maintaining a fully occupied PdH state. Interestingly, we monitored abrupt blue shifts in f_{res} at 6% < O_2 < 8% ($m = -0.5$, ③ to ④). To rationalize these unexpected blue shift, we conducted two sets of simulations by assuming that either i) Pd dehydrogenation progressed (PdH-to-Pd phase, green arrow in Figure 5b inset) or ii) β-phased PdH state was maintained keeping its intrinsic interatomic structure during the water-forming process (red arrow, Figure 5b inset). No plausible scenario can explain this blue shift unless the possibility of Pd dehydrogenation during the water-forming reactions is ruled out. As demonstrated in Figure 3d and Figure 4e, the THz signals from the geometrical alteration, including Pd expansion as a result of the Pd-PdH phase transition, are plotted in the gray area in Figure 5b. When combined, the time-lapse of the THz signals measured in each area of Figure 5b provided clues for understanding the internal lattice modulation by Pd dehydrogenation during H_2O forming reaction even under successive H_2 supply. Counterintuitive blue-shift both in measured- and simulated Δf_{res}-ΔT_{max} map provided important information regarding Pd hydrogenation and the following H_2O forming reaction over the Pd nanofilm, which dynamically underwent an abnormal dehydrogenation step (Figure S17, Supporting Information). Finally, as the O_2 concentration continued to increase, both experimental and simulation data showed an excellent agreement to follow along the previously defined H_2O forming and growth guide line ($m = 1.85$, ④ to ⑤ and ⑥).

We further set the THz measurements in the opposite way, that is, we gradually decreased the H_2 influx at the O_2 supply of 10% (Figure 5c), and plotted them in the Δf_{res}-ΔT_{max} map (Figure 5d; Figure S18, Supporting Information). From the mapped data, the interfacial O_2 adsorption process was monitored within the red zone (① to ②), followed by successive process of Pd hydrogenation (② to ③) and Pd dehydrogenation (③ to ④). We found that Pd dehydrogenation is governed by the relative ratio of H_2 to O_2. In our case, the H_2:O_2 = 7:10 condition activated the Pd dehydrogenation process (Figure 5c,d), which was in good agreement with the H_2:O_2 = 5:7 Pd dehydrogenation process (Figure 5a,b). Further studies should be conducted to define Pd dehydrogenation and to determine the relative ratio H_2/O_2. Following this scheme, above $H_2 > 4$% supply, dominant H_2O forming situations were measured (④ to ⑥, Figure 5d). Finally, when the lower hydrogen concentration became deficient for H_2O formation, the process returned to the oxygen adsorption state dominant (⑥ to ⑦) and majority of Pd surface would be covered with O adhesives. In summary, the THz nanoscopic approach enabled us to monitor the sequential process of interatomic lattice dynamics during Pd hydrogenation/dehydrogenation as well as interfacial surface chemistry, such as O_2 adsorption and H_2O formation, and their growth in a reversible and reliable manner (Figure S19, Supporting Information). A combined analysis using both experiments and simulations can fully demonstrate the robustness of the THz metachip probe for unveiling gas/metal reactions in both interatomic and interfacial scopes. This mapping method can also serve as a directional roadmap for interpreting complex molecular dynamics.

3. Conclusion

THz nanoscopic measurements enabled us to monitor the interfacial and interatomic modulation of gas-transition metals and the analysis of atomic-level lattice behaviors and their dynamics. This is advantageous for several reasons. First, the most squeezed THz field, produced effectively in ≈14 nm-wide nanogaps, significantly enhanced the incident field, enabling excellent sensing resolution down to the atomic scale. In addition, the intentionally designed asymmetric structure maximized the electrical energy absorption of the metal, resulting in the sensitive measurement of changes in the intrinsic properties of metals. The elaborately designed metasurface system with optimized dimensions and layers provides useful information (Figures 1 and 2). This covered a multi-range length scale: millimeter scale of field of view, micrometer scale of THz wavelength of light, and atomic-to-nanometer scale with superior scope resolution. Since XRD enables the tracking of interatomic fusionic gas interaction into crystalline metal lattices, our THz nanoscopic approach for transducing the gas–matter reaction into light–matter interactions provided additional information on interfacial molecular adsorption and related catalytic analysis, which has been explored using a variety of sophisticated techniques such as SPM,[19] low-energy electron microscopy (LEEM).[46] Ellipso-microscopy for surface imaging (EMSI),[47] and reflection anisotropy microscopy (RAM).[48] Second, the THz
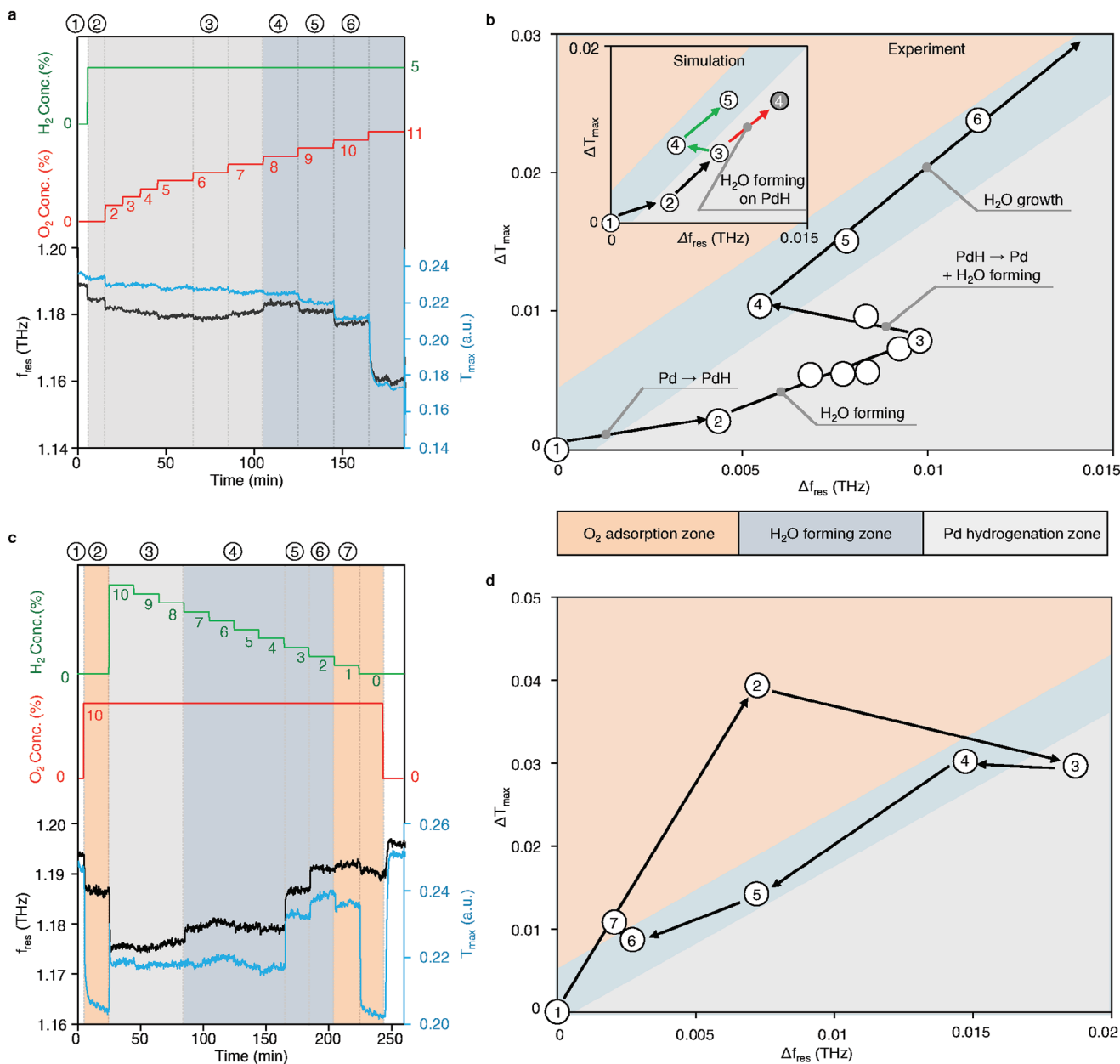
**ADVANCED
SCIENCE NEWS**

www.advancedsciencenews.com

**ADVANCED
MATERIALS**

www.advmat.de

Figure 5. THz monitoring of gas-induced complex lattice or interfacial dynamics of the Pd metal during water forming reaction. a,b) Time-lapse f_{res} (black) and T_{max} (blue) curves with increasing O_2 concentrations under 5% H_2 supply (a), and corresponding Δf_{res}-ΔT_{max} map (b). Inset shows the simulation results, including two possible scenarios of gas–metal status during water formation: either dehydrogenation (green pathway) or hydrogen fully occupied Pd lattice (red pathway). c,d) Time-lapse f_{res} and T_{max} curves with decreasing H_2 concentrations under 10% O_2 supply (c), and corresponding Δf_{res}-ΔT_{max} map (d).

wave has a 4 meV photon energy (at 1 THz); thus, it can be used to investigate flammable gases and the possible sparks that cause spontaneous explosion even at a minimal hydrogen concentration (<4% in an atmospheric environment[49]) can be avoided. In addition, the low photon energy exposed to THz nanoslots caused negligible temperature increments, enabling physicochemical analysis of the interfacial/interatomic phenomena. Third, the THz wave intrinsically showed a broad absorption spectrum for water molecules ≈1.17 THz, which can be applied for efficient investigation of H_2O-forming dynamics rather than other ultra-

broadband electromagnetic waves.[50] Real-time tracking of the hidden stages, including the hydrogenation stages (Figure 3), was possible owing to this metasurface-assisted H_2O sensitive measurement system, which discloses the initiating conditions of H_2O formation by controlling the gas composition within the chamber (Figure 4). Most importantly, the underlying process of H_2O formation by dehydrogenation was captured experimentally and has never been investigated using broadly defined optical methods (Figure 5). Given that The inter-lattice dynamics of gas–transition metals and subsequent atomic/molecular reactions

at catalytic interfaces during H_2O genesis are controversial and have not been established by different detection methods or measuring environments,[42,45] our THz nanoscope opens an alternative route for unveiling a variety of hidden stages of unknown phenomena. Our system will create a variety of opportunities, not only to clarify physics, chemistry, and applied surface science, but also to meet industrial needs by varying the composition of materials.

4. Experimental Section

Design and Fabrication of Metasurface Sensing Chips: A THz metasurface was fabricated using photolithography technique, with punctured rectangular slots with a width of $w = 500$ nm, lengths of $l = 59$ and 41μm for two types of resonances. The fabrication process is illustrated in detail in Figure S20 (Supporting Information). The adjacent slots have periods of 40 and 10 μm between them in the horizontal and vertical directions, respectively. These slot patterns were created onto a 150 nm-thick gold deposited 675 μm-thick silicon wafer (double-side-polished, undoped, and with a resistivity of $>10\,000\, \Omega$). The total number of slots were more than 35 000 ($l = 59\, \mu$m) or 48 000 (41 μm) for a whole area of 1 cm $\times$ 1 cm. They were designed to maximize the directivity of the diffracted THz signal in transmission and minimize the noise ratio from the side lobes, in turn, to enhance the sensitivity of the system. Each elementary slot had a fundamental resonance, f_{res}, of 0.97 and 1.37 THz, respectively, according to the effective refractive index of substrate. To produce effective Pd nanogaps within the nanoslots, an additional 20 nm/10 nm layer of Pd/Ti was deposited using a thermal evaporator (MHS-1800; Muhan). A polymer mixture containing 6.0 wt. % PBVE polymer (CyclAFlor Clear Chromis Technologies, USA) in a fluoro-solvent (CyclaSolv-PFC180, Chromis Technologies, USA) was spin-coated on the Pd/Ti-coated metachip at 1 200 rpm for 30 s. It was left at room temperature for 1 h and baked at 50, 80, and 180 °C for 1 h each using a hotplate, remaining a 400 nm thick PBVE film.

Time-Domain THz Spectroscopy: The broadband spectrum in the range 0.2–2.0 THz was obtained using the THz time-domain spectroscopy technique throughout the experiments (Figure S3a, Supporting Information). A femtosecond laser drives the THz optical system by exciting THz pulses and detecting the transmitted THz signals. First, an 800 nm centered laser pulse with a duration of 100 fs and a repetition rate of 80 MHz (Maitai HP, Spectra-Physics) was used. It was then divided into two paths using a beam splitter (one for THz generation and the other for detection as a probe beam). When one beam reached the THz emitter, which had a high-voltage photoconductive antenna, a THz pulse was generated and guided by parabolic mirrors. Subsequently, the transmitted waves, including the metasurface chips, passed through the gas chamber, and each gas (H_2, O_2, and N_2) was injected into the chip. Subsequently, the THz wave that diffracted through the metasurface was collected and guided again by the parabolic mirrors to the THz detector. Another probe laser beam separated from the splitter travelled through the optical delay stage toward the rear of the THz detector, that is, the ZnTe nonlinear crystal. Therefore, the simultaneous coincidence of both the THz wave and probe laser beam (picosecond level) and spot led to polarization changes in terms of the THz intensity. THz signals could be acquired indirectly using an electro-optic sampling method by measuring the polarization change in a nonlinear crystal. Consequently, the measured time-domain pulses with a shape centered at 1 ps, obtained by scanning the spatial optical delay stage, yielded the full THz pulse information (both amplitude and phase). In our experiments, the time-domain signal provided a broad time range of 0—10 ps corresponding to a delay position of 0—3 mm. The THz system was packaged and purged to prevent undesired atmospheric absorption.

Statistical Analysis: All data processing of the THz signals was handled using numerical computing software (Python). The measured THz data were acquired from nanoslot arrays with $N = 3038$. Every real-time tracking was performed with a step resolution of 3.2 s, and all data points

described using the Δf_{res}-ΔT_{max} mapping were represented as mean value (S4, Supporting Information).

Gas Control and Optical Analysis: The volumetric flow rates of N_2, O_2, and H_2 were controlled using a mass flow controller (MFC). The H_2 concentration was monitored using a hydrogen concentration analyzer (EN-600, Shanghai ENCEL Instrument Co., Ltd.) installed at the outlet of the chamber.

Supporting Information

Supporting Information is available from the Wiley Online Library or from the author.

Conflict of Interest

The authors declare no conflict of interest.

Author Contributions

Jinwoo Lee & Jongsu Lee conceived the study, fabricated the devices. G. Lee designed and conducted optical simulation. D.-S.K. assisted with device fabrication and figure configurations. Jongsu Lee controlled the gas exposure experiment and drew all the schematic figures. Jinwoo Lee and G. Lee conducted entire optical measurement. Y.-S.R. and M.S. wrote the manuscript and supervised work. All authors contributed to the scientific discussion and manuscript revisions.

Data Availability Statement

The data that support the findings of this study are available from the corresponding author upon reasonable request.

[1] J. I. Avila, R. J. Matelon, R. Trabol, M. Favre, D. Lederman, U. G. Volkmann, A. L. Cabrera, *J. Appl. Phys.* **2010**, *107*, 023504.

[2] T. Driscoll, G. O. Andreev, D. N. Basov, S. Palit, S. Y. Cho, N. M. Jokerst, D. R. Smith, *Appl. Phys. Lett.* **2007**, *91*, 062511.

[3] J. Lloyd-Hughes, T.-I. Jeon, *J. Infrared, Millimeter, Terahertz Waves* **2012**, *33*, 871.

[4] X. Yang, X. Zhao, K. Yang, Y. Liu, Y. Liu, W. Fu, Y. Luo, *Trends Biotechnol.* **2016**, *34*, 810.

[5] S.-H. Lee, S. Shin, Y. Roh, S. J. Oh, S. H. Lee, H. S. Song, Y.-S. Ryu, Y. K. Kim, M. Seo, *Biosens. Bioelectron.* **2020**, *170*, 112663.

[6] J. Lv, S. Shen, L. Chen, Y. Zhu, S. Zhuang, *PhotoniX* **2023**, *4*, 28.

[7] T. Kang, Y.-M. Bahk, D.-S. Kim, *Nanophotonics* **2020**, *9*, 435.

[8] D. K. Gramotnev, S. I. Bozhevolnyi, *Nat. Photonics* **2010**, *4*, 83.

[9] M. A. Seo, H. R. Park, S. M. Koo, D. J. Park, J. H. Kang, O. K. Suwal, S. S. Choi, P. C. M. Planken, G. S. Park, N. K. Park, Q. H. Park, D. S. Kim, *Nat. Photonics* **2009**, *3*, 152.

[10] Y. Roh, S.-H. Lee, J. Kwak, H. S. Song, S. Shin, Y. K. Kim, J. W. Wu, B.-K. Ju, B. Kang, M. Seo, *Sens. Actuators, B* **2022**, *352*, 130993.

[11] L. Xu, J. Xu, J. Liu, D. Lin, J. Lei, B. Zhou, Y. Shen, X. Deng, *Sens. Actuators, B* **2022**, *367*, 132016.

[12] E. S. Yu, S. H. Lee, G. Lee, Q. H. Park, A. J. Chung, M. Seo, Y. S. Ryu, *Adv. Sci.* **2021**, *8*, 2170058.

[13] F. A. A. Nugroho, P. Bai, I. Darmadi, G. W. Castellanos, J. Fritzsche, C. Langhammer, J. Gómez Rivas, A. Baldi, *Nat. Commun.* **2022**, *13*, 5737.

[14] E. Maeda, S. Mikuriya, K. Endo, I. Yamada, A. Suda, J.-J. Delaunay, *Appl. Phys. Lett.* **2009**, *95*, 133504.

[15] M. Johansson, E. Skúlason, G. Nielsen, S. Murphy, R. M. Nielsen, I. Chorkendorff, *Surf. Sci.* **2010**, *604*, 718.

[16] B. D. Adams, A. Chen, *Mater. Today* **2011**, *14*, 282.

[17] A. Houari, S. F. Matar, V. Eyert, *J. Appl. Phys.* **2014**, *116*, 173706.

[18] A. Tittl, P. Mai, R. Taubert, D. Dregely, N. Liu, H. Giessen, *Nano Lett.* **2011**, *11*, 4366.

[19] G. Ertl, W. Sesselmann, *Surf. Sci.* **1989**, *217*, 383.

[20] W. Yuan, B. Zhu, X.-Y. Li, T. W. Hansen, Y. Ou, K. Fang, H. Yang, Z. Zhang, J. B. Wagner, Y. Gao, Y. Wang, *Science* **2020**, *367*, 428.

[21] K. Sytwu, M. Vadai, F. Hayee, D. K. Angell, A. Dai, J. Dixon, J. A. Dionne, *Science* **2021**, *371*, 280.

[22] D. Narehood, S. Kishore, H. Goto, J. Adair, J. Nelson, H. Gutierrez, P. Eklund, *Int. J. Hydrogen Energy* **2009**, *34*, 952.

[23] Y. Fukai, N. Okuma, *Phys. Rev. Lett.* **1994**, *73*, 1640.

[24] M. Vadai, D. K. Angell, F. Hayee, K. Sytwu, J. A. Dionne, *Nat. Commun.* **2018**, *9*, 4658.

[25] Y.-M. Bahk, S. Han, J. Rhie, J. Park, H. Jeon, N. Park, D.-S. Kim, *Phys. Rev. B* **2017**, *95*, 075424.

[26] K. R. Kim, J.-S. Noh, J. M. Lee, Y. J. Kim, W. Lee, *J. Mater. Sci.* **2011**, *46*, 1597.

[27] J. H. Kang, J.-H. Choe, D. S. Kim, Q.-H. Park, *Opt. Express* **2009**, *17*, 15652.

[28] J. Kang, D. Kim, M. Seo, *Nanophotonics* **2018**, *7*, 763.

[29] S. S. Das, G. Kopnov, A. Gerber, *AIP Adv.* **2020**, *10*, 065129.

[30] S. Wagner, A. Pundt, *Int. J. Hydrogen Energy* **2016**, *41*, 2727.

[31] P. Ferrin, S. Kandoi, A. U. Nilekar, M. Mavrikakis, *Surf. Sci.* **2012**, *606*, 679.

[32] N. J. J. Johnson, B. Lam, B. P. Macleod, R. S. Sherbo, M. Moreno-Gonzalez, D. K. Fork, C. P. Berlinguette, *Nat. Mater.* **2019**, *18*, 454.

[33] X. W. Zhou, T. W. Heo, B. C. Wood, V. Stavila, S. Kang, M. D. Allendorf, *J. Appl. Phys.* **2018**, *123*, 225105.

[34] S. Wagner, M. Hamm, A. Pundt, *Scr. Mater.* **2013**, *69*, 756.

[35] O. Dankert, A. Pundt, *Appl. Phys. Lett.* **2002**, *81*, 1618.

[36] A. Kawasaki, S. Itoh, K. Shima, K. Kato, H. Ohashi, T. Ishikawa, T. Yamazaki, *Phys. Chem. Chem. Phys.* **2015**, *17*, 24783.

[37] F. A. A. Nugroho, I. Darmadi, L. Cusinato, A. Susarrey-Arce, H. Schreuders, L. J. Bannenberg, A. B. Da Silva Fanta, S. Kadkhodazadeh, J. B. Wagner, T. J. Antosiewicz, A. Hellman, V. P. Zhdanov, B. Dam, C. Langhammer, *Nat. Mater.* **2019**, *18*, 489.

[38] R. Griessen, N. Strohfeldt, H. Giessen, *Nat. Mater.* **2016**, *15*, 311.

[39] J. Zhu, H. Li, X. Li, J. Li, *J. Chem. Phys.* **2022**, *157*, 134707.

[40] J. Lee, E. S. Yu, T. Kim, I. S. Kim, S. Chung, S. J. Kwak, W. B. Lee, Y. Pak, Y. S. Ryu, *PhotoniX* **2023**, *4*, 20.

[41] M. A. El-Okazy, L. Liu, C. P. Junk, E. Kathmann, W. White, S. E. Kentish, *J. Memb. Sci.* **2021**, *634*, 119401.

[42] L.-G. Petersson, H. M. Dannetun, I. Lundström, *Surf. Sci.* **1985**, *161*, 77.

[43] J. Roques, C. Lacaze-Dufaure, C. Mijoule, *J. Chem. Theory Comput.* **2007**, *3*, 878.

[44] C. Nyberg, C. G. Tengstål, *J. Chem. Phys.* **1984**, *80*, 3463.

[45] H. M. Dannetun, D. Söderberg, I. Lundström, L.-G. Petersson, *Surf. Sci.* **1985**, *152*, 559.

[46] T. U. Clausthal, *Ultramicroscopy* **1985**, *17*, 57.

[47] J. Dicke, H.-H. Rotermund, J. Lauterbach, *J. Opt. Soc. Am. A* **2000**, *17*, 135.

[48] J. Dicke, P. Erichsen, J. Wolff, H. H. Rotermund, *Surf. Sci.* **2000**, *462*, 90.

[49] P. Ngene, T. Radeva, M. Slaman, R. J. Westerwaal, H. Schreuders, B. Dam, *Adv. Funct. Mater.* **2014**, *24*, 2374.

[50] J. Zhou, X. Rao, X. Liu, T. Li, L. Zhou, Y. Zheng, Z. Zhu, *AIP Adv.* **2019**, *9*, 035346.